Subaqueous volcanism in the Paleo-Pacific Ocean based on Jurassic basaltic tuff and pillow basalt in the Raohe Complex, NE China

3 authors, including:

Mingdao Sun
Chinese Academy of Sciences
10 PUBLICATIONS   **153** CITATIONS

SEE PROFILE

Yi-Gang Xu
Chinese Academy of Sciences
278 PUBLICATIONS   **11,715** CITATIONS

SEE PROFILE

Some of the authors of this publication are also working on these related projects:

Craton failure using geodynamical modelling View project

Stable isotopes View project

Subaqueous volcanism in the Paleo-Pacific Ocean based on Jurassic basaltic tuff and pillow basalt in the Raohe Complex, NE China

SUN MingDao[1*], XU YiGang[1] & CHEN HanLin[2]

[1] *State Key Laboratory of Isotope Geochemistry, Guangzhou Institute of Geochemistry, Chinese Academy of Sciences, Guangzhou 510640, China;*

[2] *Earth Science College, Zhejiang University, Hangzhou 310027, China*

Abstract On-land records of subaqueous explosive volcanic eruptions are rarely reported. To understand this phenomenon and discuss its global significance, we studied the geochronology and geochemistry of basaltic tuff and pillow basalt in the Raohe Complex, NE China. The basaltic tuff consists of well-sorted vitreous, crystal (mostly clinopyroxene), and minor lithic fragments. It is characterized by a high MgO (15.7–15.9%) content and zero Eu anomalies (Eu/Eu*=99–102). The tuff erupted at 172 ±1 Ma based on SHRIMP zircon U-Pb dating, coeval with the previously reported age of the pillow basalt. The pillow basalt has intermediate MgO content and weakly negative Eu anomalies (Eu/Eu*=90–99). Based on immobile trace element discrimination, the basaltic tuff and pillow basalt belong to alkali basalt displaying an OIB-type trace element pattern, and consistent Nd isotope signatures of $\varepsilon_{Nd}(t)$ =4.4–6.2, indicating an identical mantle source. The pillow basalt has coupled Sr-Nd isotopic values, whereas the basaltic tuff has significantly higher initial $^{87}Sr/^{86}Sr$ values that are similar to synchronous seawater. This indicates that the elemental exchange between the mantle-derived material and seawater most likely occurred in a subaqueous explosive volcanic eruption, rather than in an effusive eruption. Detailed calculations suggest that the high efficiency of the Sr-isotope exchange between seawater and the mantle-derived material triggered by a subaqueous explosive volcanic eruption is likely one of the main reasons for the rapid decrease of the global seawater $^{87}Sr/^{86}Sr$ value.

Keywords Raohe Complex, Subaqueous volcanism, Jurassic, Paleo-Pacific Ocean, Seawater Sr isotope

1. Introduction

Subaqueous volcanism, which makes up 85% of global volcanism (White et al., 2003; Arculus, 2011), is important to understand the paleo-environment and tectonic evolution. However, because of subduction processes and the destruction of oceanic plates, only some of the subaqueous volcanic remains in the paleo-oceans are accreted onto continental margins and preserved within accretionary complexes. The eruption style, including effusive and explosive, is controlled by the interior and exterior conditions of the volcano. The interior conditions, including magma (basic or acidic, alkaline or sub-alkaline) viscosity and volatile component (CO_2 and H_2O) content, are similar to subaerial volcanos. However, the exterior conditions vary and are controlled by water property and depth. Compared with air, water has higher density, greater viscosity, higher heat capacity, and thermal conductivity, which result in different conditions during the subaqueous eruption (McBirney, 1963; Cas, 1992). Subaqueous effusive eruptions favor the formation of pillow lavas and hyaloclastic rocks (Pallister et al., 1989; Wright, 2001; Garcia et al., 2007; Porreca et al., 2014). Modern ef-

*Corresponding author (email: smd@zju.edu.cn)

fusive eruptions can be observed and recorded, although this is expensive, because of the deep dive technology that has been developed in recent years and because the effusive eruption is smooth and constant (Resing et al., 2011). Ancient effusive eruptions can be preserved in accretionary complexes on land and are therefore ideally suited to identify oceanic closure and suture zones. Subaqueous explosive eruptions (Cas, 2006) preferentially produce pyroclastic rocks (Sheridan and Wohletz, 1981; Wohletz and Sheridan, 1983; Schneider, 2000; Head and Wilson, 2003; Allen et al., 2007; Helo et al., 2013; Kutterolf et al., 2014). Modern submarine explosive eruptions are more expensive to observe directly (Embley et al., 2006; Sohn et al., 2008; Chadwick et al., 2008), and are poorly understood because they occur abruptly and intermittently. Ancient subaqueous explosive eruptions are also rarely reported.

Previous studies suggest that a subaqueous explosive eruption is unlikely to form at depths greater than 500 meters because of the high exterior pressure (McBirney, 1963; Cas, 1992). However, this hypothesis has been challenged by new observations. Clague et al. (2000) studied the Lo′ihi seamount and concluded that explosive eruptions can occur at a depth of 1200 m. Embley et al. (2006) and Chadwick et al. (2008) presented a video record of a subaqueous explosive eruption at a depth of 700 m in the Mariana arc. Resing et al. (2011) and Arculus (2011) reported a subaqueous explosive eruption at 1200 m depth in the Tonga arc. Sohn et al. (2008) investigated pyroclastic rocks at 4000 m depth on the Gakkel Ridge in the Arctic Ocean. Clague et al. (2009) collected glassy lava fragments from over 450 sites along the Juan de Fuca Ridge in the Pacific Ocean. Iezzi et al. (2014) reported submarine explosive eruptions in the Mediterranean Sea. The above observations show that subaqueous explosive eruptions potentially occur in volatile-rich island arc volcanism and in volatile-poor ridge volcanism, and in shallow and deep water. Furthermore, the observations of modern subaqueous explosive eruptions are mostly from ridges and arcs, but rarely from seamounts. This may be because of the relative inactivity of the current plumes compared with the Permian, Jurassic, and Cretaceous.

In this paper, we report SHRIMP U-Pb zircon geochronological and geochemical results for pillow basalt and basaltic tuff in the Raohe Complex, NE China. We present an ancient intra-oceanic coeval effusive-explosive eruption to better understand subaqueous volcanism within the Paleo-Pacific Ocean, its tectonic evolution history, ocean-lithosphere interactions, and global change.

2.   Geological background, sample location and petrography

2.1   Geological background

The study area is located in the Wandashan Orogen, NE China (Figure 1a). It is also named Nadanhada Terrane (Mizutani and Kojima, 1992), and consists of the Yuejinshan and Raohe complexes, and Early Cretaceous continental arc igneous rocks (Zhou et al., 2014; Sun et al., 2015). The Yuejinshan Complex contains Yuejinshan metamorphic belt greenschist and marble, and Dongfanghong SSZ-type ophiolite. The Raohe Complex contains Triassic to Jurassic intra-oceanic sedimentary and volcanic rocks as the accretionary prism, and a Late Jurassic to Early Cretaceous marine-facies fore-arc basin from terrestrial sources. This study focuses on the Mid-Jurassic Dalingqiao Formation volcanic rocks in the Raohe Complex, including basaltic tuff and pillow basalt.

2.2   Sample locations

The basaltic tuff samples were collected 12 km southwest of the Dumuhe Village (46°17′52.6″N, 133°25′44.1″E) (Figure 1b, c). The outcrop is about 10 m long along the northern side of a small muddy road. Six tuff samples (13RH03-1 to 13RH03-6) were randomly collected.

The pillow basalt samples were collected from a quarry 17 km southwest of Raohe Town (46°46′58.1″N; 133°46′24.2″E) (Figure 1b) on the eastern side of the road. The diameter of the pillows is about 30–50 cm. Seven basalt samples (09RH08-1 to 09RH08-7) were randomly collected.

2.3   Petrography

Figure 2 shows the photomicrograph of the basaltic tuff and pillow basalt samples.

The basaltic tuff consists of ~55% crystal fragments, ~40% vitreous fragments, and ~5% lithic fragments (<5%), and tuffaceous matrix (<5%) (Figure 2a, b). The fragments are well sorted, clast-supported, angular, and have a major axis diameter of ~100 μm. The fragments are mostly clinopyroxene (~70%). There are also some chlorite (15–20%), hornblende, serpentine, talc, epidote, actinolite, chromite, plagioclase, calcite, and quartz. The vitreous fragments are brown in color and angular in shape. They have similar size as the crystal fragments, and have experienced various degrees of devitrification and chloritization. The vitreous fragments are also characterized by locally directional distribution features (Figure 2c). The lithic fragments are rounded basaltic tuff 0.5–2 mm in size (Figure 2d). They may have erupted earlier from the same host rock. The matrix mainly consists of chloritic fine-grained volcanic ash. These petrography signatures indicate that the tuff was formed in a subaqueous explosive volcanic eruption and subaqueous deposition, instead of in sedimentation from a terrestrial source, "yellow-green muddy feldspar siltstone", as previously reported (HBGMR, 1987a, b; Filippov and Kemkin, 2003).
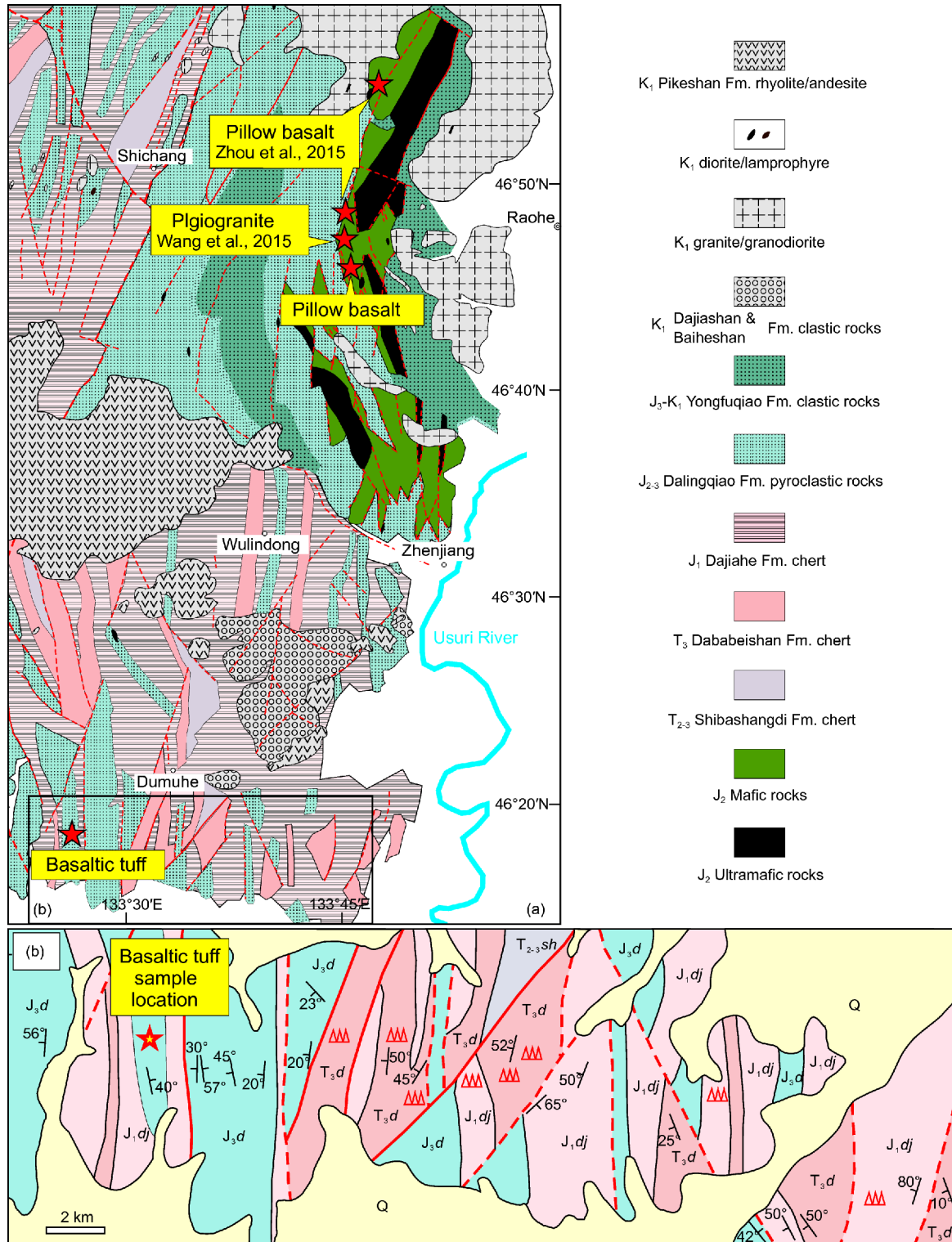
Figure 1   Regional geological map of the Raohe Complex. (a) Geological map of the Raohe Complex with sample locations. (b) Geological map of the exposed area of the basaltic tuff after HBGMR (1987a, b).

The basalt samples consist of about 20% clinopyroxene and 80% plagioclase, with intergranular-intersertal texture. The lateral alteration occurred in various degrees, mainly through chloritization and carbonization (Figure 2e, f).

3.   Methods

3.1   *In-situ* mineral analysis

The *in-situ* electron microprobe analysis was conducted at

Figure 2   Photomicrographs of the basaltic tuff ((a)–(d)) and basalt ((e), (f)). (a) and (e) were photographed using cross-polarized light; (b), (c), (d) and (f) were photographed using plane-polarized light.
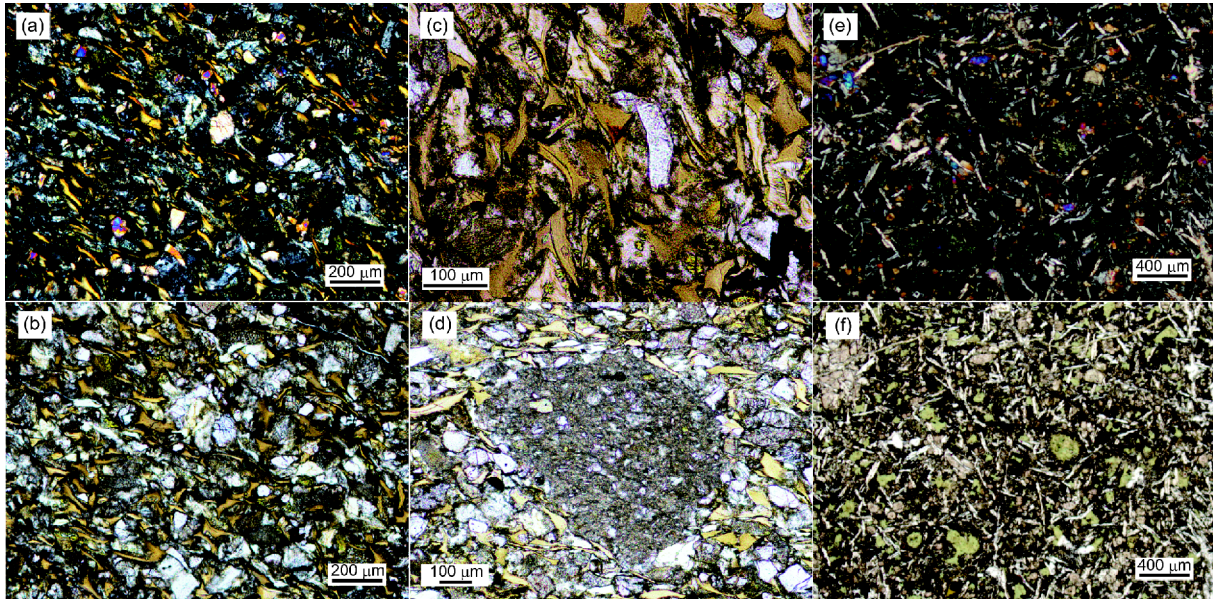
the State Key Laboratory of Isotope Geochemistry, Guangzhou Institute of Geochemistry, Chinese Academy of Sciences (SKLIG-GIGCAS) using JEOL JXA-8230 and standard analytical procedures. The quantitative detection limit is ~100 ppm. The laser Raman Spectrum analysis was conducted at the Earth Science College, Zhejiang University, using LabRAM HR evolution 800 combined with the Olympus BX41 microscope. The analytical procedure follows Frezzotti et al. (2012).

3.2   Whole rock geochemical analysis

Six tuff and seven basalt samples were collected and crushed to 200-mesh size in an agate mill for whole-rock geochemical analysis. Major elements were analyzed using X-ray fluorescence spectrometry (XRF) at SKLIG-GIGCAS (samples 13RH03-x) and at the Center of Modern Analysis, Nanjing University (samples 09RH08-x). Trace element analyses were carried out at SKLIG-GIGCAS, using a Finnigan Element Inductively-Coupled Plasma Mass Spectrometer (samples 13RH03-x); and at the State Key Laboratory for Mineral Deposits Research, Nanjing University (SKLMDR-NU) using a PerkinElmer Elan 6000 ICP-MS (samples 09RH08-x). The Sr-Nd isotopes were analyzed at SKLIG-GIGCAS using a Thermo Finnigan Neptune MC-ICP-MS (samples 13RH03-x); and at the SKLMDR-NU using a Thermal Ionization Mass Spectrometer (TIMS) Finnigan Triton TI (samples 09RH08-x). Sr isotopic ratios were normalized to a $^{86}Sr/^{88}Sr$ ratio of 0.1194, and the Nd-isotopic ratios to a $^{146}Nd/^{144}Nd$ ratio of 0.7219. The chemical laboratory procedures and the calculations of the initial Sr and Nd isotope ratios were according to Jiang et al. (1999)

and Guo et al. (2010).

3.3   Zircon U-Pb dating

An approximately 10 kg of rock was collected from tuff sample 13RH03-1 for zircon separation. About 1000 grains of zircon crystals were extracted by crushing, and heavy liquid and magnetic separation at the Langfang Geological Services Corporation, Hebei Province, China, and then mounted along with the TEMORA standard (Black et al., 2003). Cathodoluminescence (CL) images were taken using a Philips XL30 Scanning Electron Microscope at Curtin University. SHRIMP U-Pb dating was performed using a SHRIMP II ion microprobe at Curtin University following standard procedures (Nelson et al., 1995). Six scans were used through the mass stations for data collection. Standard BR266 (559 Ma, U = 909 ppm) (Stern et al., 2001) was used for the U concentration and age calibration, and TEMORA (417 Ma) (Black et al., 2003) was used to monitor analytical conditions. Ages and concordia diagrams were calculated using the SQUID 1.03 (Ludwig, 2001) and ISOPLOT 3.0 (Ludwig, 2003) programs.

4.   Results

4.1   Mineral composition of the basaltic tuff

The crystal fragments in the tuff were analyzed using an electron probe. The data are presented in Table 1. The results suggest that the crystal fragments are mainly clinopyroxene grains, most of which plot in the diopside and augite area (Figure 3a). These grains have Raman spectrum peaks at

Table 1   Electron microprobe analysis results of the crystal fragments in the tuff (%)[a]

No.	K_2O	Na_2O	SiO_2	TiO_2	Al_2O_3	FeO	MgO	MnO	CaO	Cr_2O_3	Total	Mineral
1	0.0	0.4	45.7	3.4	7.9	9.5	11.3	0.2	21.4	0.1	99.9	Cpx
2	0.0	0.5	45.4	2.9	7.6	8.5	11.7	0.1	22.7	0.1	99.5	Cpx
3	0.0	0.4	46.3	3.0	6.9	7.5	11.9	0.1	23.2	0.2	99.6	Cpx
4	0.0	0.5	46.0	2.6	7.2	8.1	12.1	0.1	22.2	0.6	99.6	Cpx
5	0.0	0.4	46.7	3.4	6.4	7.7	12.2	0.2	22.7	0.3	99.8	Cpx
6	0.0	0.4	47.2	2.4	6.0	8.5	12.5	0.1	22.5	0.1	99.7	Cpx
7	0.0	0.4	48.1	2.0	5.4	7.8	12.8	0.1	22.5	0.5	99.5	Cpx
8	0.0	0.4	47.7	2.2	5.7	7.7	12.9	0.1	22.6	0.2	99.7	Cpx
9	0.0	0.4	47.5	2.1	5.5	7.6	13.0	0.1	22.9	0.6	99.7	Cpx
10	0.0	0.3	47.1	2.3	6.0	8.4	13.1	0.1	22.0	0.1	99.5	Cpx
11	0.0	0.3	49.7	1.6	4.2	6.7	13.6	0.1	23.1	0.2	99.6	Cpx
12	0.0	0.4	50.0	1.6	4.0	5.9	14.0	0.1	22.4	1.2	99.7	Cpx
13	0.0	0.4	50.1	1.7	4.0	6.0	14.3	0.1	22.3	1.0	99.9	Cpx
14	0.0	0.3	50.7	1.0	3.5	4.9	14.4	0.1	23.2	1.4	99.6	Cpx
15	0.0	0.3	50.9	1.2	3.3	5.2	14.5	0.1	23.8	0.8	100.0	Cpx
16	0.0	0.3	51.0	1.2	3.1	6.6	14.6	0.2	22.2	0.2	99.6	Cpx
17	0.0	0.3	51.4	1.3	2.8	7.4	14.7	0.1	21.7	0.1	99.7	Cpx
18	0.0	0.3	50.3	1.1	3.6	5.0	15.1	0.1	23.1	1.2	99.9	Cpx
19	0.0	0.3	50.9	1.1	3.1	5.9	15.2	0.1	21.9	0.9	99.5	Cpx
20	0.0	0.3	51.7	1.0	2.6	5.8	15.4	0.1	21.9	0.9	99.8	Cpx
21	0.0	0.3	51.6	0.9	2.7	5.1	15.5	0.1	22.3	1.0	99.5	Cpx
22	0.0	0.2	52.6	0.9	2.1	6.0	15.9	0.1	21.1	0.5	99.5	Cpx
23	0.0	0.2	51.9	1.0	2.1	6.3	16.0	0.2	21.3	0.4	99.5	Cpx
24	0.0	0.0	0.3	1.4	12.8	19.2	12.4	0.2	0.2	49.0	95.9	chromite
25	0.0	0.0	0.1	4.0	16.1	31.8	10.9	0.3	0.0	35.7	99.2	chromite
26	0.0	1.3	44.8	3.5	6.9	14.3	8.7	0.5	18.6	0.0	98.9	hornblende
27	0.0	1.3	46.0	3.2	5.8	13.6	9.2	0.7	18.9	0.0	98.7	hornblende
28	0.0	1.4	45.8	2.7	6.7	14.3	9.4	0.6	18.6	0.0	99.6	hornblende
29	0.0	0.0	76.0	0.1	7.7	4.0	1.3	0.0	9.0	0.0	98.3	epidote
30	0.0	0.0	36.9	0.1	12.4	17.4	17.7	0.1	0.9	0.1	85.8	epidote
31	0.0	0.0	99.4	0.0	0.0	0.0	0.0	0.0	0.0	0.0	99.5	quartz
32	0.0	0.0	0.1	45.9	0.1	50.2	0.1	3.6	0.1	0.0	100.1	ilmenite
33	0.1	0.0	30.4	28.0	3.6	8.0	4.1	0.8	20.0	0.1	95.0	sphene

a) Oxide content is given as percent, Cpx: clinopyroxene.

325/390/668/1008 indicating typical clinopyroxene (Figure 3b). As shown in the scatter plots of $Mg^{\#}$, Al_2O_3, TiO_2 vs. SiO_2 of the clinopyroxene grains, with the increase in SiO_2 content from ~44% to ~53%, the $Mg^{\#}$ value increases from 63 to 85 (Figure 3c), the Al_2O_3 value increases from 63 to 85 (Figure 3d), and the TiO2 content decreases from ~3.5 % to ~0.5% (Figure 3e). The large range of variability may be related to quenching crystallization under subaqueous volcanism (Guilbaud et al., 2007). In addition to clinopyroxene, minerals including amphibole, serpentine, talc, epidote, titanite, actinolite, chromite, plagioclase, calcite, and quartz are also observed using micro- and electron scopes (Table 1).

These are common minerals in basalts and their hydrothermally-altered products.

4.2   Major and trace elements

The major, trace, and rare earth element analysis results of the six tuff and seven basalt samples are presented in Table 2.

The tuff samples measured 47.4–48.2% SiO_2, 0.15–0.67% Na_2O, and 0.09–0.11% K_2O. The low alkali content is potentially caused by hydrothermal alteration (Figure 4a), rather than indicating a sub-alkaline series. The Figure 4b suggests that the tuff belongs to alkali basalt. The high MgO
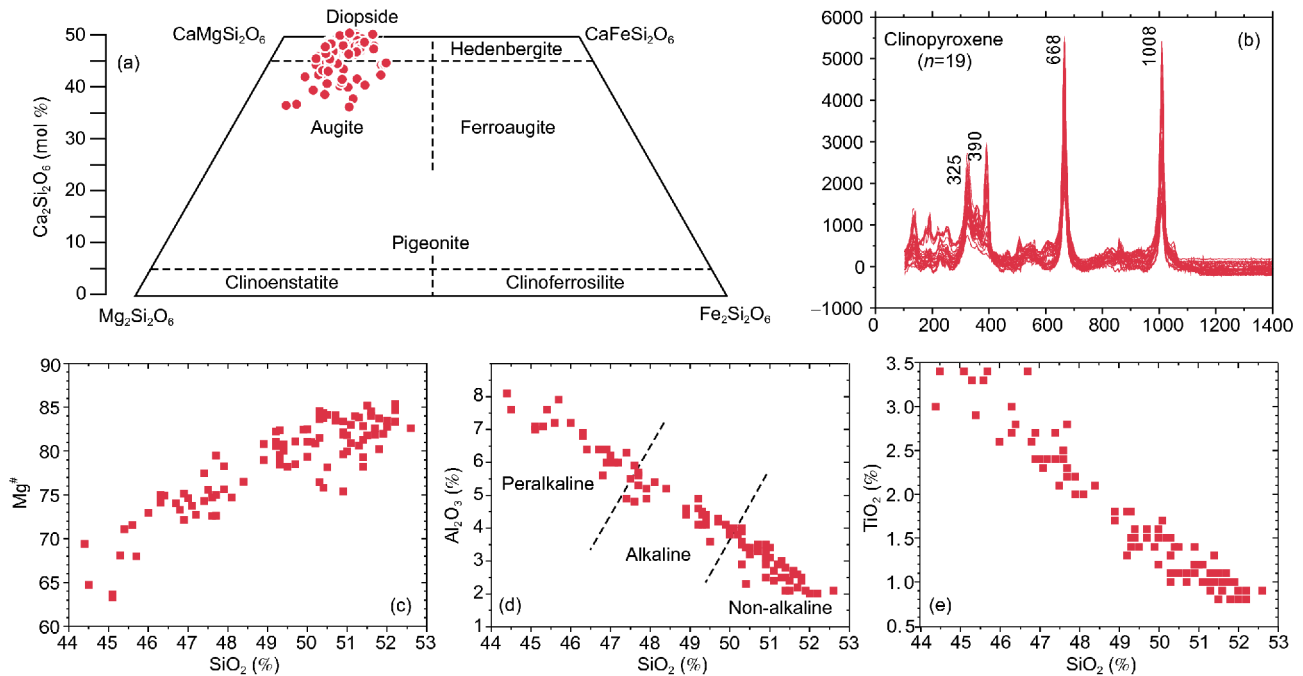
Figure 3   *In-situ* analysis results of the clinopyroxene fragments in the tuff using an electron microprobe and laser Raman spectroscopy. (d) is after Kushiro (1960) and Le Bas (1962).

(15.72–15.92%), $Mg^{\#}$ (70–71) and Ni (549.2–582.5 ppm) content indicates that the magma is relatively primary without significant fractionation (Figure 4c, d).

The tuff sample REE content ranged from 99 to 105 ppm, with high LREE/HREE ratios ($(La/Yb)_N$ of 8.1–8.3) and no Eu anomalies (Eu/Eu^*=98–102). This again indicates relatively primary magma without significant fractionation (Figure 4e). In the spider diagram (element Rb, Ba, K, Sr, and Pb are mobile and not shown), the basalt is also characterized by the enrichment of High Field Strength Elements (HFSE) Nb and Ta (Figure 7b), displaying an OIB-type signature. The significant depletion of Sr (4.4–5.6 ppm), Ba (8.9–9.8 ppm), and K_2O (~0.1%) is likely caused by hydrothermal alteration (Figure 4g, h).

The basalt samples contain from 43.3–52.8% SiO_2, 0.48–4.99% Na_2O, and 0.12–3.54% K_2O. The large range of K_2O and Na_2O values is caused by hydrothermal alteration, instead of igneous processes. Because of lateral alteration and mobile K_2O and Na_2O, application of the TAS diagram (Figure 4a) is not possible to show the magma series of the tuff. The immobile elements Zr/Ti *vs*. Nb/Y diagram (Figure 4b) suggest that the samples fall into the alkali basalt field. The relatively low MgO (5.79–14.41%), $Mg^{\#}$ (49–63), and Ni (78.2–135.0 ppm) content indicates that the magma experienced moderate crystallization fractionation (Figure 4c, d).

The REE content of the basalt samples ranges from 110 to 144 ppm, with high LREE/HREE ratios ($(La/Yb)_N$ of 5.5–8.0) and no to slightly negative Eu anomalies (Eu/Eu^*=90–

99) (Figure 4e). In the spider diagram (elements Rb, Ba, K, Sr, and Pb are mobile and not shown), the basalt is characterized by the enrichment of HFSE Nb and Ta, displaying an OIB-type pattern. Caused by the different extent of alteration, there is significant variability in the Rb (2.9–33.0 ppm), Ba (43–552 ppm), Sr (134–678 ppm), and K_2O (0.12–3.44%) content.

In summary, the pillow basalt and basaltic tuff are both alkali. The magma of the pillow basalt experienced moderate fractionation, whereas the magma of the tuff is more primary. The tuff and basalt have similar REE and spider diagram patterns demonstrating OIB signatures. The mobile elements Rb, Ba, Sr, and K (Table 2) are not used in the lateral tectonic discrimination and mantle source analyses.

4.3   Sr-Nd isotopes

The whole rock Sr and Nd isotopic data are listed in Table 3.

The initial Sr-Nd isotopic compositions are all back-calculated to 170 Ma. The basalt has initial $^{87}Sr/^{86}Sr$ ratios ranging from 0.703553 to 0.703776, and $\varepsilon_{Nd}(t)$ values ranging from 4.4 to 6.1, indicating an OIB-type mantle source (Figure 5). The tuff has significantly higher initial $^{87}Sr/^{86}Sr$ ratios ranging from 0.706491 to 0.706706, but similar $\varepsilon_{Nd}(t)$ values ranging from 5.8 to 6.2. This indicates that the tuff was derived from a similar source with the pillow basalt, producing their comparable Nd isotope values, whereas the Sr element is mobile during alteration and the original Sr isotope of the tuff is not preserved.

Table 2 Major, trace, and rare earth element analysis results[a]

	Pillow basalt							Basaltic tuff					
	RH08-1	RH08-2	RH08-3	RH08-4	RH08-5	RH08-6	RH08-7	RH03-1	RH03-2	RH03-3	RH03-4	RH03-5	RH03-6
SiO_2	47.51	46.22	45.14	46.63	41.66	51.41	43.90	45.37	44.94	44.96	44.52	44.69	44.61
TiO_2	3.07	2.70	2.75	2.79	2.69	2.42	2.97	2.43	2.26	2.41	2.33	2.39	2.33
Al_2O_3	12.46	10.85	10.94	10.49	9.41	10.41	11.63	8.94	8.77	8.53	8.74	8.57	8.63
$Fe_2O_3^T$	11.70	13.32	14.25	13.04	16.46	10.55	14.91	12.25	12.32	12.27	12.49	12.41	12.40
MnO	0.16	0.17	0.17	0.18	0.20	0.13	0.18	0.17	0.16	0.17	0.17	0.17	0.17
MgO	5.58	10.78	11.20	10.72	13.86	6.58	11.40	14.80	14.95	14.98	14.93	14.91	14.87
CaO	10.44	8.68	8.51	10.71	10.52	11.56	7.84	9.22	9.86	10.25	10.29	10.36	10.16
Na_2O	4.81	0.50	0.50	1.66	0.47	3.84	0.51	0.63	0.35	0.19	0.14	0.17	0.18
K_2O	0.27	3.44	2.97	1.12	0.62	0.12	2.77	0.10	0.10	0.09	0.09	0.09	0.09
P_2O_5	0.34	0.29	0.28	0.29	0.29	0.28	0.26	0.26	0.26	0.26	0.27	0.26	0.26
LOI	4.01	3.38	3.69	2.60	4.04	3.09	4.18	5.72	5.97	5.80	5.89	5.74	6.06
Total	100.36	100.32	100.41	100.25	100.23	100.40	100.56	99.89	99.96	99.90	99.86	99.77	99.76
Na_2O+K_2O	5.27	4.06	3.59	2.85	1.13	4.06	3.40	0.77	0.48	0.29	0.25	0.28	0.28
$Mg^\#$	48.6	61.6	60.9	62.0	62.5	55.3	60.2	70.5	70.6	70.7	70.3	70.4	70.4
V	265	275	288	263	301	239	279	275	280	269	268	271	269
Cr	108	417	422	616	549	630	638	1221	1245	1243	1206	1215	1244
Mn	1234	1359	1394	1552	1753	1100	1552	1318	1300	1313	1316	1339	1315
Co	33.0	46.0	51.4	51.0	54.9	45.1	53.3	61.6	61.2	62.7	65.4	65.2	63.3
Ni	87.6	87.6	94.8	105.5	135.0	78.2	133.2	549.2	568.8	582.5	571.0	581.9	572.2
Cu	120.0	82.7	90.3	114.1	95.9	99.9	121.1	114.0	113.1	106.4	106.0	106.6	105.6
Zn	72.1	101.8	111.8	87.1	214.6	48.3	107.9	105.2	105.4	100.7	102.1	104.6	101.1
Ga	19.8	15.4	15.8	17.0	19.8	16.7	19.2	15.4	16.1	16.0	16.2	16.3	16.1
Rb	11.3	31.9	33.0	10.3	12.1	2.9	23.9	6.8	7.3	7.9	7.9	8.0	7.9
Sr	434	678	654	515	134	252	535	118	107	95	93	95	95
Y	28.0	22.9	21.5	22.7	25.6	23.5	25.1	18.2	18.5	17.9	17.9	18.2	17.9
Zr	198.8	178.1	184.4	159.3	174.1	154.4	173.2	148.6	152.3	148.5	146.5	147.7	146.1
Nb	23.8	23.7	29.6	21.9	22.5	19.9	23.5	23.6	23.7	23.1	23.2	23.3	23.0
Cs	2.64	3.41	4.29	1.66	3.34	1.01	3.37	3.85	4.10	4.26	4.27	4.29	4.25
Ba	71	552	482	195	142	43	462	69	67	62	62	63	63
La	22.6	17.5	16.2	23.9	20.9	18.8	21.9	17.2	17.2	16.5	16.3	16.5	16.3
Ce	51.5	41.5	37.8	47.1	44.1	40.9	46.2	39.0	38.5	36.4	36.2	36.7	36.0
Pr	7.58	6.11	5.95	6.51	6.37	6.18	6.88	5.35	5.27	5.08	5.06	5.12	5.07
Nd	33.0	26.7	25.6	29.1	27.7	26.0	28.8	22.1	22.0	21.1	21.0	21.3	21.1
Sm	7.14	6.25	5.98	6.34	6.42	5.72	6.81	5.28	5.29	5.05	5.02	5.07	5.02
Eu	2.03	2.02	1.84	1.89	1.95	1.68	2.06	1.63	1.66	1.63	1.63	1.64	1.62
Gd	6.51	6.16	5.65	6.11	6.07	5.65	6.23	4.93	5.00	4.79	4.72	4.84	4.77
Tb	1.02	0.90	0.90	0.92	1.01	0.91	1.05	0.76	0.76	0.73	0.73	0.74	0.73
Dy	5.51	5.19	4.74	4.75	5.50	4.85	5.44	4.15	4.16	3.99	4.04	4.04	4.02
Ho	0.98	0.93	0.85	0.89	0.97	0.86	0.97	0.78	0.79	0.74	0.75	0.76	0.75
Er	2.51	2.31	2.23	2.27	2.60	2.19	2.68	1.91	1.91	1.81	1.81	1.84	1.83
Tm	0.41	0.38	0.35	0.36	0.39	0.36	0.41	0.25	0.25	0.24	0.25	0.25	0.24
Yb	2.47	2.29	2.08	2.15	2.32	2.05	2.33	1.49	1.49	1.44	1.43	1.43	1.43
Lu	0.34	0.34	0.31	0.31	0.34	0.28	0.35	0.22	0.21	0.21	0.20	0.21	0.20
Hf	5.37	4.86	5.45	4.72	4.75	4.26	4.81	3.87	3.90	3.76	3.74	3.76	3.72
Ta	1.71	1.64	2.06	1.49	1.57	1.37	1.98	1.51	1.52	1.46	1.48	1.48	1.48
Pb	3.24	3.92	6.78	4.54	2.03	2.71	3.54	3.36	3.03	2.69	2.50	2.69	2.64
Th	3.05	2.48	2.27	2.42	2.73	2.64	2.77	1.98	1.97	1.88	1.89	1.89	1.89
U	0.71	0.52	0.56	0.55	0.54	0.44	0.61	0.49	0.50	0.47	0.47	0.48	0.48
Eu/Eu^*	0.91	0.99	0.97	0.93	0.95	0.90	0.96	0.98	0.99	1.01	1.02	1.01	1.01
Th/Yb	1.24	1.08	1.09	1.12	1.18	1.29	1.19	1.33	1.32	1.31	1.32	1.33	1.32
Nb/Yb	9.64	10.35	14.28	10.18	9.70	9.69	10.07	15.89	15.90	16.05	16.22	16.30	16.08
TiO_2/Yb	1.24	1.18	1.33	1.30	1.16	1.18	1.27	1.64	1.52	1.68	1.63	1.68	1.62
Zr/Y	7.10	7.79	8.59	7.01	6.79	6.57	6.90	8.16	8.21	8.31	8.18	8.11	8.16
Zr/Ti	0.012	0.011	0.010	0.010	0.011	0.011	0.011	0.010	0.010	0.010	0.010	0.010	0.010

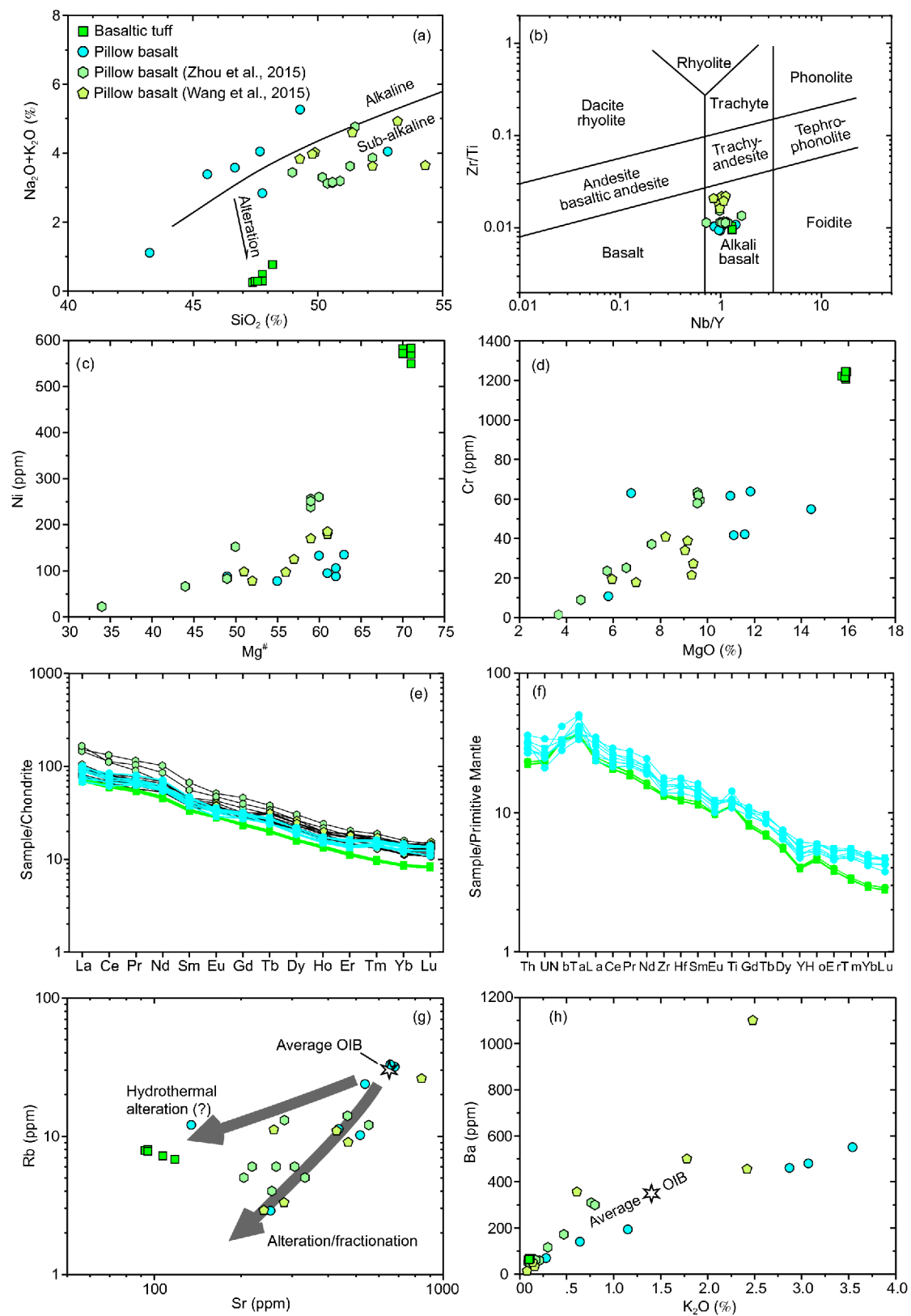a) Major element is in %, trace element is in ppm.

Figure 4 Bulk major and trace element geochemical signatures of the basaltic tuff and basalt. (a) TAS diagram; (b) Zr/Ti *vs.* Nb/Y discrimination diagram; (c) Ni *vs.* Mg# scatter diagram; (d) Cr *vs.* MgO scatter diagram; (e) chondrite-normalized rare earth element pattern diagram; (f) primitive mantle normalized spider diagram; (g) Rb *vs.* Sr scatter diagram; (h) Ba *vs.* K₂O scatter diagram. The chondrite and primitive mantle values are based on Sun and McDonough (1989).

Table 3   Sr-Nd isotopic analysis results

Sample	Rb (ppm)	Sr (ppm)	$^{87}Rb/^{86}Sr$	$^{87}Sr/^{86}Sr$	$\pm2\sigma$	$(^{87}Sr/^{86}Sr)_i$	Sm (ppm)	Nd (ppm)	$^{147}Sm/^{144}Nd$	$^{143}Nd/^{144}Nd$	$\pm2\sigma$	$\varepsilon_{Nd}(t)$
09RH08-1	11	434	0.08	0.703932	5	0.703750	7	33	0.1309	0.512872	2	5.99
09RH08-2	32	678	0.14	0.704006	3	0.703677	6	27	0.1417	0.512802	5	4.40
09RH08-3	33	654	0.15	0.703984	4	0.703631	6	26	0.1414	0.512804	14	4.44
09RH08-4	10	515	0.06	0.703900	10	0.703761	6	29	0.1316	0.512866	4	5.86
09RH08-5	12	134	0.26	0.704185	2	0.703553	6	28	0.1401	0.512887	7	6.09
09RH08-6	3	252	0.03	0.703856	3	0.703776	6	26	0.1331	0.512835	3	5.22
09RH08-7	24	535	0.13	0.703986	3	0.703674	7	29	0.1429	0.512828	3	4.88
13RH03-1	7	118	0.17	0.707110	7	0.706706	5	22	0.1446	0.512892	4	6.09
13RH03-2	7	107	0.2	0.707145	6	0.706672	5	22	0.1453	0.512896	4	6.15
13RH03-3	8	95	0.24	0.707177	8	0.706600	5	21	0.1445	0.512895	4	6.15
13RH03-4	8	93	0.24	0.707238	6	0.706649	5	21	0.1446	0.512893	4	6.11
13RH03-5	8	95	0.24	0.707079	6	0.706491	5	21	0.1440	0.512878	4	5.83
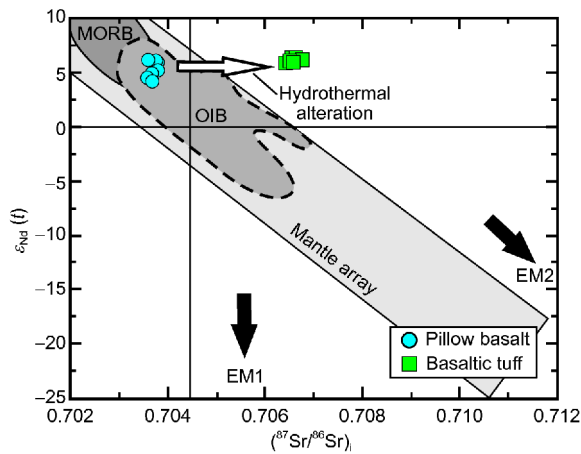
Figure 5   Plot of $\varepsilon_{Nd}(t)$ vs. initial $^{87}Sr/^{86}Sr$ of the pillow basalt and basaltic tuff.

4.4   Zircon U-Pb geochronology

The results of the zircon SHRIMP U-Pb dating is presented in Table 4.

The zircons from the basaltic tuff sample 13RH03-1 are mostly 50 μm in diameter. The zircon grains are transparent and pale yellow. Their CL images show unclear oscillatory zonation, possibly because of their basaltic origin (Figure 6a). Fifteen zircon grains were analyzed. The measured U and Th concentrations vary from 259 to 1547 ppm and from 138 to 984 ppm, respectively. The Th/U ratios ranged from 0.39 to 1.26, and therefore all the grains are magmatic. Fifteen analyses gave a concordance age of 172 ± 1 Ma (MSWD = 2.7) (Figure 6b), representing the eruption age of the tuff.

The age of the pillow basalt has been well dated. Zhou et al. (2014) reported that the zircon LA ICP-MS U-Pb age of the pillow basalt is 167±1 Ma. Therefore, the eruption of the pillow lavas may have been slightly later than that of the tuff. Wang et al. (2015) reported a zircon LA ICP-MS U-Pb age of

the anorthosite and plagiogranite of 169±2 and 167±4 Ma, respectively. This further confirms that the Raohe Complex preserves abundant records of Mid-Jurassic magmatism.

5.   Discussion

5.1   Mantle source and tectonic implication

The basaltic tuff and pillow basalt have similar REE and spider diagram patterns (Figure 4e, f), indicating enrichment of Nb and Ta, and OIB-type signatures. In Figure 4b, they both plot in the alkali basalt field. In Figure 7a and b, discrimination diagrams, the basalt and tuff again plot in the OIB field. In Figure 7c, they plot in the Within Plate Basalts field. They also have similar $\varepsilon_{Nd}(t)$ values ranging from 4.4 to 6.2, further indicating an OIB-type mantle source (Figure 5).

Wang et al. (2015) suggested that the regional pillow basalt derived from the low degree partial melting (<5%) of the garnet peridotite mantle. However, their reported trace element Zr (244–410 ppm) and Hf of the basalt are significantly higher than the results of this study (Zr = 146–199 ppm) or Zhou et al. (2014). Thus, their Lu/Hf vs. La/Sm diagram is not applicable to determine the partial melting degree and mantle source. If the Raohe basalts were derived from the partial melting of the mantle peridotite, based on the Sm/Yb vs. La/Yb diagram (after Xu et al., 2005), they potentially originated from the high degree partial melting of garnet peridotite (10–15%).

In summary, the basaltic rocks in the Raohe Complex belong to OIB-type alkali basalt, with a consistent mantle source. They were formed within the oceanic plate and accreted to the continental margin as part of the accretionary prism. The accretion occurred at or before ~140 Ma because the basalts are covered by Late Jurassic to Early Cretaceous fore arc basins and are intruded by Early Cretaceous granites

Table 4 Zircon SHRIMP U-Pb dating results of the basaltic tuff sample RH03-1 [a]

Sample	U (ppm)	Th (ppm)	Th/U	^{206}Pb (ppm)	$^{206}Pb_c$ (%)	$^{204}Pb^*/^{206}Pb^*$	±%	$^{207}Pb^*/^{235}U$	±%	$^{206}Pb^*/^{238}U$	±%	error	%Disc-ordant	$^{207}Pb^*/^{235}U$		$^{206}Pb^*/^{238}U$	
														Age(Ma)	1σ	Age(Ma)	1σ
RH03-1-01	532	522	0.98	16	1.4	0.0007	27	0.17321	8	0.02691	2	0.2	5	163	11	171	3
RH03-1-02	532	404	0.76	15	1.6	0.0009	25	0.15940	10	0.02684	2	0.2	12	151	14	171	3
RH03-1-03	289	285	0.99	8	4.4	0.0024	20	0.14230	20	0.02596	2	0.1	18	136	25	165	3
RH03-1-04	259	234	0.90	8	0.6	0.0003	58	0.18278	6	0.02673	2	0.3	1	171	10	170	3
RH03-1-05	545	408	0.75	15	0.8	0.0004	33	0.17314	5	0.02692	2	0.3	5	163	8	171	3
RH03-1-06	459	579	1.26	15	0.4	0.0002	50	0.17541	5	0.02660	2	0.3	3	165	7	169	3
RH03-1-07	571	481	0.84	17	1.2	0.0006	27	0.16860	7	0.02735	2	0.2	9	159	10	174	3
RH03-1-08	390	235	0.60	11	0.5	0.0003	50	0.18539	5	0.02669	2	0.3	2	174	8	170	3
RH03-1-09	318	198	0.62	9	0.3	0.0002	71	0.18149	5	0.02719	2	0.3	2	170	7	173	3
RH03-1-10	358	138	0.39	9	0.7	0.0004	45	0.18379	6	0.02678	2	0.3	1	172	9	170	3
RH03-1-11	887	478	0.54	25	0.0	0.0000	100	0.19292	2	0.02749	1	0.7	3	180	4	175	3
RH03-1-12	1005	718	0.71	28	0.6	0.0003	29	0.17327	4	0.02695	2	0.4	5	163	5	172	2
RH03-1-13	1063	753	0.71	31	0.2	0.0001	45	0.17942	3	0.02752	1	0.5	4	168	5	175	2
RH03-1-14	1547	984	0.64	46	0.2	0.0001	41	0.20111	2	0.02890	1	0.7	2	187	4	184	3
RH03-1-15	457	482	1.05	14	0.9	0.0005	35	0.17567	6	0.02705	2	0.3	4	165	9	172	3

a) Error is 1-sigma; Pb_c and Pb^* indicate common and radioactive lead, respectively.
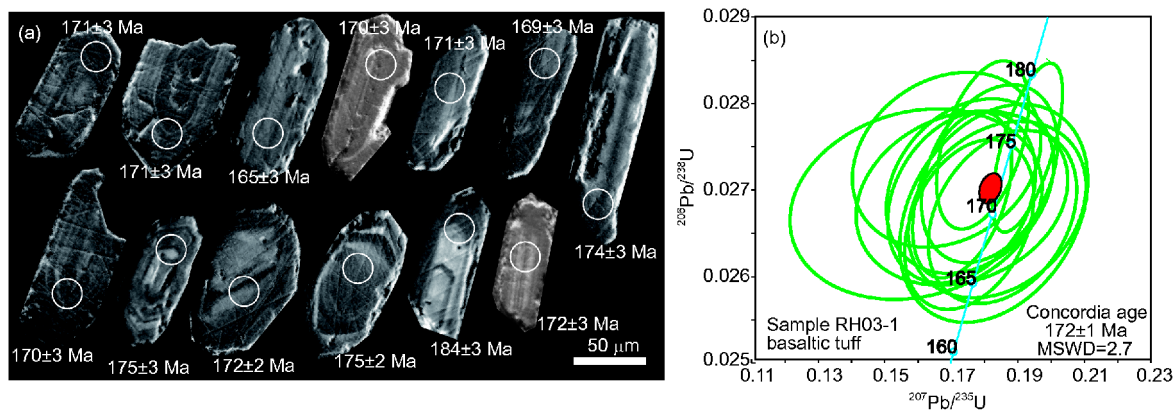
Figure 6 Zircon CL images of the tuff sample RH03-1 (a) and zircon SHRIMP U-Pb concordia diagram (b).

(Sun et al., 2015).

Mid-Jurassic oceanic island basalt accretion occurred widely in the circum-Pacific orogenic belts (Xenophontos and Osozawa, S., 2004; Ichiyama and Ishiwatari, 2005; Wakita, 2012; Buchs et al., 2013), and Paleo-Pacific Ocean volcanism in the Mid-Jurassic was active potentially because of the super-plume (Kimura et al., 1994; Safonova et al., 2009; Ballmer et al., 2010; Safonova and Santosh, 2014; Ichiyama et al., 2014).

5.2 Subaqueous explosive eruption and seawater-volcanic interaction

The interaction between seawater and volcanic materials is mainly reflected in the alteration characteristics of rocks. The basaltic tuff and pillow basalt experienced alteration. The tuff has secondary minerals, such as, serpentine and chlorite and an ignition loss of 5.7–6.1%. The pillow basalt has

chlorite and calcite with an ignition loss of 2.6–4.2%.

The geochemical signature indicates that the pillow basalt experienced various degrees of alteration, including (1) low alkali content, (2) modified Ba and K_2O content, and (3) partial activity of the Rb and Sr elements. In the immobile element Zr/Ti vs. Nb/Y discrimination diagram (Figure 4b), the basalts all plot in the alkali basalt section. However, some samples did not plot in this field in the TAS diagram because of their very low total alkali. In Figure 4h, the Ba and K_2O display a positive linear relationship. Furthermore, the pillow basalt from different locations has different slopes of the linear trend line. The Rb content of the basalt is significantly lower than the average OIB, and cannot be interpreted based on the fractionation of olivine, pyroxene, or plagioclase, but was most likely caused by alteration. Although the Rb and Sr elements are active, the measured $^{87}Sr/^{86}Sr$ value varied slightly and was coupled with the $^{143}Nd/^{144}Nd$ values (Table 3). This suggests that the Sr isotopic system of the basalt is
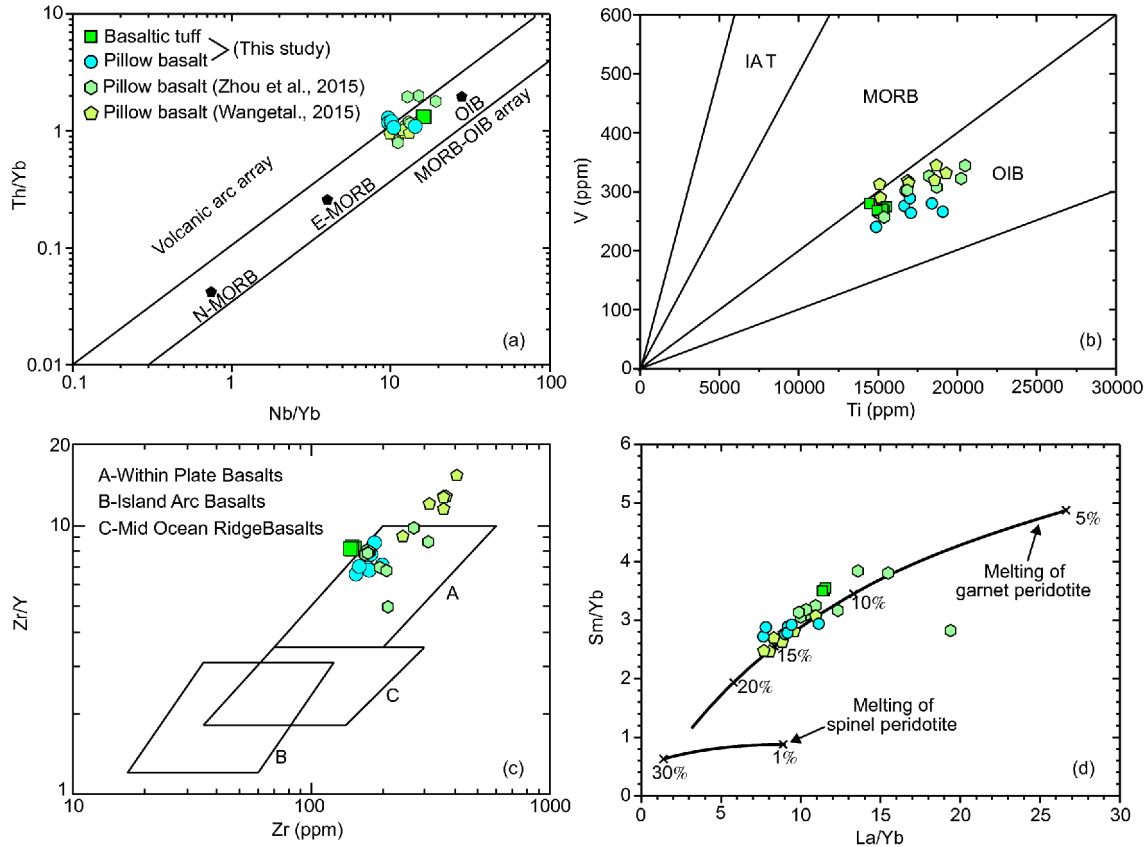
Figure 7 Tectonic and mantle source discrimination diagrams of the basaltic tuff and pillow basalt. After Shervais (1982) and Xu et al. (2005).

not destroyed. The low Rb/Sr ratio and the relatively young age of the basalt guaranteed negligible change in the initial $^{87}Sr/^{86}Sr$ value because of the variability of the Rb and Sr content. Thus the initial $^{87}Sr/^{86}Sr$ and $\varepsilon_{Nd}(t)$ values are coupled and plot in the OIB area (Figure 5).

The alteration signature of the basaltic tuff is not consistent with the pillow basalt. The tuff has higher ignition loss, and potentially experienced greater hydrothermal alteration. It has an extremely low alkali content (0.25–0.77%; Figure 4a) that is significantly less than that of common alkali basalt determined using trace element discrimination (>3%). In Figure 4h and g, the tuff has no linear relationships similar to those of the lava. The Rb and Sr content of the tuff is clearly different from the range of oceanic island basalt. The $^{87}Sr/^{86}Sr$ ratio of the tuff is about 0.7071. The initial $^{87}Sr/^{86}Sr$ ranges between approximately 0.7065–0.7067, higher than the value of the pillow lava of ~0.7040. These signatures suggest that the tuff experienced a higher degree of alteration than the basalt, and a different alteration type. The Sr isotopic system of the tuff was destroyed potentially because of the effect of seawater.

Previous studies provide abundant data on the Sr isotopic ratio of global seawater from the late Paleozoic to the Cenozoic, providing an illustration of the variability of global seawater Sr isotopes (Figure 8). The basaltic tuff has a

$^{87}Sr/^{86}Sr$ ratio similar to ~172 Ma old seawater (Figure 8). The tuff and pillow basalt experienced accretion and on-land alteration, but display different alteration results. Thus, we propose that the tuff may have been altered during the explosive eruption, whereas the lava was not. This view is consistent with observations of modern volcanic activity. For example, Mielke et al. (2015) found that the alteration degree is highly related to the physical properties of rocks, and the increase in the porosity and permeability from lava and volcanic breccia to volcanic tuff indicates that the tuff is more likely being altered. Seawater alteration occurred after the deposition of the erupted tuffaceous materials, and also during the explosive eruption. Significant alteration occurs when the erupted material and seawater mix in the 'convective region' and at the 'mixing surface' (Figure 9) as a result of the power released by the subaqueous explosive eruption (Censi et al., 2010). Therefore, the Sr element exchange between seawater and the subaqueous volcanic materials most likely occurred during explosive, rather than effusive, eruptions.

5.3 Chemical exchange model between volcanic material and seawater

The $^{87}Sr/^{86}Sr$ ratio increase of global seawater is thought to
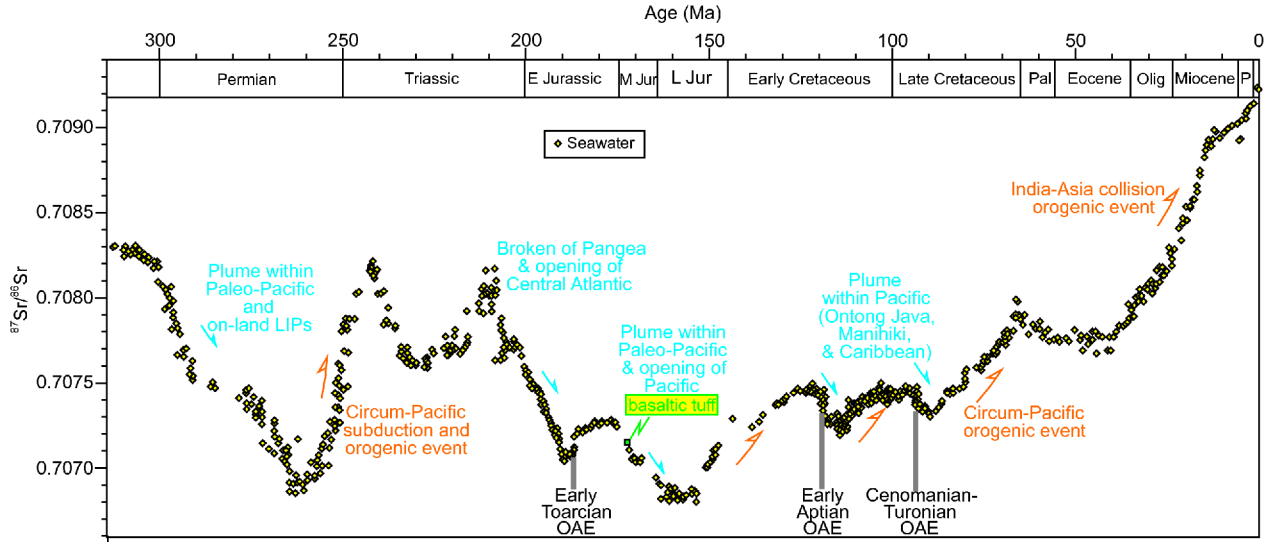
Figure 8   Global seawater Sr isotopic variation curve and major geological events. After Bruckschen et al. (1995), Jones and Jenkyns (2001), Korte et al. (2003) and Wierzbowski et al. (2012).
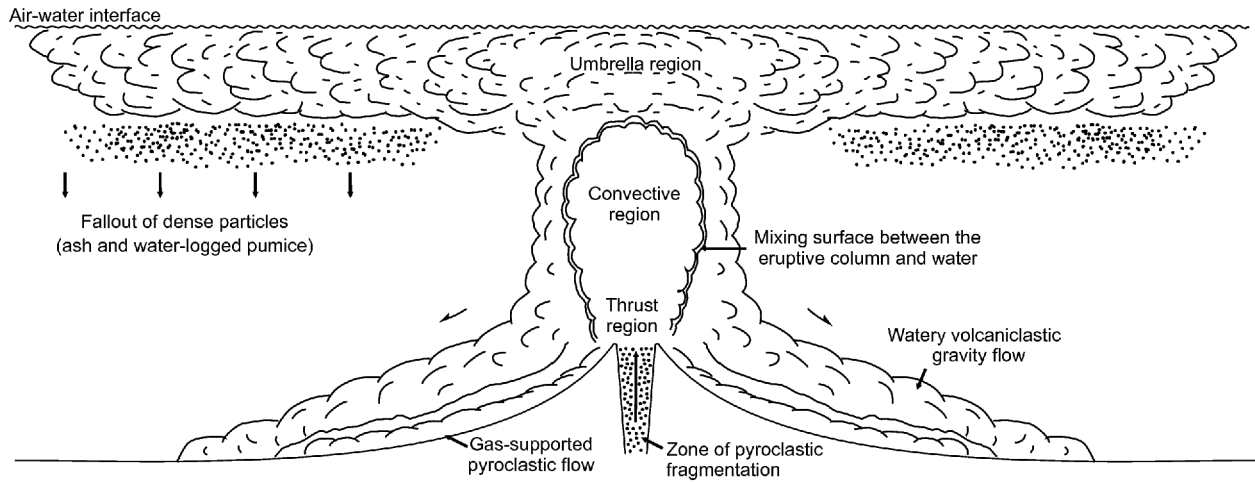

Figure 9   Synthetic model of subaqueous explosive volcanic eruptions. After Kokelaar and Busby (1992), Kano et al. (1996) and Schneider et al. (2000).

be caused by the increased input of continental material, whereas its decrease has various causes, including decrease in river water flux, decrease in riverine $^{87}Sr/^{86}Sr$ ratios, and/or the increase in the hydrothermal alteration of oceanic basalts (Richter et al., 1992; Jones and Jenkyns, 2001). For example, the seawater $^{87}Sr/^{86}Sr$ ratio decrease during the Mid-Jurassic was thought to be related to the increase in oceanic volcanism (Wierzbowski et al., 2012).

The variability of the $^{87}Sr/^{86}Sr$ value of the basaltic tuff of the Raohe Complex suggests strontium exchange with seawater. However, the effusive product pillow basalt retains the Sr isotopic characteristics of its mantle source, and seawater can change the chemical composition of the basaltic tuff. Therefore, can large submarine volcanic eruptions affect the chemical composition of global seawater?

Given that global seawater of age t_i has a Sr content of $Sr_{seawater\_ti}$ with an isotopic ratio of

$$\alpha_{ti} =^{87} Sr_{\_ti} /^{86} Sr_{\_ti}, \tag{1}$$

and given that the elemental addition of Sr by subaqueous volcanism is Sr_{input_ti} with an isotopic ratio:

$$\beta_{ti} =^{87} Sr_{\_input\_ti} /^{86} Sr_{\_input\_ti}, \tag{2}$$

set constant $\mu=(^{88}Sr_{\_ti} +^{86} Sr_{\_ti} +^{84} Sr_{\_ti})/^{86}Sr_{\_ti}=9.431757$,

$$
\begin{aligned}
Sr_{seawater\_ti} &=^{88} Sr_{\_ti} +^{87} Sr_{\_ti} +^{86} Sr_{\_ti} +^{84} Sr_{\_ti} \\
&= 8.375209 \times^{86} Sr_{\_ti} + \alpha_{ti} \times^{86} Sr_{\_ti} +^{86} Sr_{\_ti} \\
&\quad +0.056548 \times^{86} Sr_{\_ti} \\
&= (\alpha_{ti} + \mu) \times^{86} Sr_{\_ti}. \tag{3}
\end{aligned}
$$

The variability of the seawater Sr isotopic ratio caused by volcanic material follows the function:

Age (Ma)	α_{ti}	α_{ti+1}	$Sr_{\_input\_ti}$ (10^{13}t)	Eruption mass (10^{15}t)	Eruption rate (m/Ma$\times 10^6$ km^2)
175–160	0.7073	0.7068	0.18	2.75	61.2
210–190	0.7081	0.7071	0.33	5.05	84.1
280–260	0.7075	0.7069	0.21	3.21	53.5
300–290	0.7081	0.7075	0.18	2.73	90.3

$$\frac{\left(^{87}Sr_{\_ti} + ^{87}Sr_{\_input\_ti}\right)}{\left(^{86}Sr_{\_ti} + ^{86}Sr_{\_input\_ti}\right)} = \frac{^{87}Sr_{\_ti+1}}{^{86}Sr_{\_ti+1}}. \tag{4}$$

Substituting α_{ti}, β_{ti}, and μ into eq. (4), we have

$$Sr_{\_input\_ti} = \frac{\left[(\beta_{ti} + \mu)/(\alpha_{ti} + \mu)\right]}{\left[(\alpha_{ti+1} - \beta_{ti})/(\alpha_{ti} - \alpha_{ti+1})\right]}$$
$$\times Sr_{seawater\_ti}. \tag{5}$$

Assume that the additional volcanic material has OIB-type elemental and isotopic signatures (between the depleted and enriched mantle) with a Sr content of ~660 ppm and a $^{87}Sr/^{86}Sr$ value β_{ti} of 0.7035 (Sun and McDonough, 1989). The historical global seawater volume and Sr content are similar to the present, with a volume of 1.5×10^{18} t (Charette and Smith, 2010) and a Sr content of 8 ppm. Thus, the $Sr_{seawater\_ti}$ is constant at 1.2×10^{13}t, and α_{ti} and α_{ti+1} in eq. (5) are independent variables, the $Sr_{\_input\_ti}$ is a dependent variable, and the remainder are constants.

Based on the global seawater Sr isotopic variation curve (Figure 8) (Bruckschen et al., 1995; Jones and Jenkyns, 2001; Korte et al., 2003; Wierzbowski et al., 2012), the input of additional Sr element can be calculated based on different t_i and t_{i+1} values and using eq. (5). The eruption mass (10^{15} t) required can be calculated based on the average Sr content of the erupted material of 660 ppm. The eruption rate (m/Ma $\times 10^6$ km^2) can be calculated using a tuff density of 3 t/m^3. The order of magnitude '10^6 km^2' is common for large igneous provinces (LIP). For example, the area of Ontong Java LIP is ~4.9×10^6 km^2.

As shown in Table 5, four typical stages of rapid seawater $^{87}Sr/^{86}Sr$ decrease (300–290, 280–260, 210–190 and 175–160 Ma) require an average eruption rate of 90.3, 53.5, 84.1, and 61.2 m /Ma$\times 10^6$ km^2, respectively. Therefore, a 90 m/Ma $\times 10^6$ km^2 eruption rate of additional subaqueous explosive eruptions is sufficient for a rapid $^{87}Sr/^{86}Sr$ decrease in seawater.

Assuming that the area of the ancient and present oceanic surfaces are equal at about 3.6×10^8 km^2, the eruption rate of 90 m/Ma $\times 10^6$ km^2 indicates a 5 m thick tuff layer covering a 5% area of the global ocean floor in one million years. This order of magnitude is consistent with geological observations of interlayered tuff in chert, turbidite, and limestones present in the accretionary complex (HBGMR, 1987a, b; Filippov and Kemkin, 2003; Kamata et al., 2012; Stanton

and Alderson, 2013; Ikeda and Tada, 2014; Sun et al., 2015). Therefore, the subaqueous explosive volcanic eruption, which caused efficient chemical exchange between the mantle-derived material and seawater, is one of the main reasons for the rapid decrease in the $^{87}Sr/^{86}Sr$ ratio of global seawater.

In conclusion, the global seawater Sr isotopic variability can be controlled by major oceanic events of subaqueous volcanism, such as, plume and super oceanic plate spreading (Figure 8). Specifically, the rapid $^{87}Sr/^{86}Sr$ ratio decrease during events in the Permian, Early to Mid-Jurassic, and Cretaceous were likely related to the plume and large igneous provinces in the Paleo-Pacific Ocean and the opening of the modern Pacific and Atlantic (Timm et al., 2011; Safonova and Santosh, 2014).

6.   Conclusions

We applied petrological, zircon SHRIMP U-Pb, major and trace elemental, and Sr-Nd isotopic analyses of pillow basalt and basaltic tuff to evaluate their mantle source and tectonic settings. Combining the results with previous studies and calculations from a model of the chemical exchange between volcanic material and seawater, we reach the following conlusions.

(1) The basaltic tuff in the Raohe Complex has a zircon U-Pb age of 172±1 Ma, coeval with the pillow basalt with both forming in the Middle Jurassic. They are the product of subaqueous explosive and effusive eruptions, respectively.

(2) The pillow basalt and basaltic tuff belong to OIB-type alkali basalt and were potentially derived from the high-degree partial melting of a garnet peridotite mantle. The magma of the tuff is relatively primary, whereas the magma of the pillow basalt is more fractionated.

(3) The Sr-isotope exchange is more efficient between the volcanic material and seawater in an explosive eruption than in an effusive eruption. The efficient chemical exchange between the mantle-derived material and seawater, caused by a subaqueous explosive eruption, is one of the main reasons for the rapid decrease of the $^{87}Sr/^{86}Sr$ ratio of global seawater.

References

Allen S R, Hayward B W, Mathews E. 2007. A facies model for a submarine volcaniclastic apron: The Miocene Manukau Subgroup, New Zealand. Geol Soc Am Bull, 119: 725–742

Arculus R. 2011. Submarine volcanism: Deeply explosive. Nat Geosci, 4: 737–738

Ballmer M D, Ito G, van Hunen J, Tackley P J. 2010. Small-scale sublithospheric convection reconciles geochemistry and geochronology of 'Superplume' volcanism in the western and south Pacific. Earth Planet Sci Lett, 290: 224–232

Black L P, Kamo S L, Allen C M, Aleinikoff J N, Davis D W, Korsch R J, Foudoulis C. 2003. TEMORA 1: A new zircon standard for Phanerozoic U-Pb geochronology. Chem Geol, 200: 155–170

Bruckschen P, Bruhn F, Veizer J, Buhl D. 1995. isotopic evolution of Lower Carboniferous seawater: Dinantian of western Europe. Sediment Geol, 100: 63–81

Buchs D M, Pilet S, Cosca M, Flores K E, Bandini A N, Baumgartner P O. 2013. Low-volume intraplate volcanism in the Early/Middle Jurassic Pacific basin documented by accreted sequences in Costa Rica. Geochem Geophys Geosyst, 14: 1552–1568

Cas R A F. 1992. Submarine volcanism; eruption styles, products, and relevance to understanding the host-rock successions to volcanic-hosted massive sulfide deposits. Economic Geol, 87: 511–541

Cas R A F. 2006. Explosive mafic volcanism. J Volcanol Geothermal Res, 155: 1–2

Censi P, Randazzo L A, Zuddas P, Saiano F, Aricò P, Andò S. 2010. Trace element behaviour in seawater during Etna's pyroclastic activity in 2001: Concurrent effects of nutrients and formation of alteration minerals. J Volcanol Geotherm Res, 193: 106–116

Chadwick W W, Cashman K V, Embley R W, Matsumoto H, Dziak R P, de Ronde C E J, Lau T K, Deardorff N D, Merle S G. 2008. Direct video and hydrophone observations of submarine explosive eruptions at NW Rota-1 volcano, Mariana arc. J Geophys Res-Sol Earth, 113: B08S10

Charette M, Smith W. 2010. The Volume of Earth's Ocean. Oceanography, 23: 112–114

Clague D A, Davis A S, Bischoff J L, Dixon J E, Geyer R. 2000. Lava bubble-wall fragments formed by submarine hydrovolcanic explosions on Lōʻihi Seamount and Kīlauea Volcano. Bull Volcanol, 61: 437–449

Clague D A, Paduan J B, Davis A S. 2009. Widespread strombolian eruptions of mid-ocean ridge basalt. J Volcanol Geotherm Res, 180: 171–188

Cole R B, Decelles P G. 1991. Subaerial to submarine transitions in early Miocene pyroclastic flow deposits, southern San Joaquin basin, California. Geol Soc Am Bull, 103: 221–235

Embley R W, Chadwick W W, Baker E T, Butterfield D A, Resing J A, de Ronde C E J, Tunnicliffe V, Lupton J E, Juniper S K, Rubin K H, Stern R J, Lebon G T, Nakamura K I, Merle S G, Hein J R, Wiens D A, Tamura Y. 2006. Long-term eruptive activity at a submarine arc volcano. Nature, 441: 494–497

Filippov A N, Kemkin I V. 2003. Clastic rocks from Permian and Triassic cherty sequences in Sikhote Alin and Japan. Lithol Mineral Resour, 38: 36–47

Frezzotti M L, Tecce F, Casagli A. 2012. Raman spectroscopy for fluid inclusion analysis. J Geochem Expl, 112: 1–20

Garcia M O, Haskins E H, Stolper E M, Baker M. 2007. Stratigraphy of the Hawaiʻi Scientific Drilling Project core (HSDP2): Anatomy of a Hawaiian shield volcano. Geochem Geophys Geosyst, 8: Q02G20–37

Guilbaud M N, Blake S, Thordarson T, Self S. 2007. Role of Syn-eruptive Cooling and Degassing on Textures of Lavas from the AD 1783–1784 Laki Eruption, South Iceland. J Petrol, 48: 1265–1294

Guo F, Fan W, Gao X, Li C, Miao L, Zhao L, Li H. 2010. Sr-Nd-Pb isotope

mapping of Mesozoic igneous rocks in NE China: Constraints on tectonic framework and Phanerozoic crustal growth. Lithos, 120: 563–578

HBGMR (Heilongjiang Bureau of Geology and Mineral Resources). 1987a. 1:200 000 Regional Geological Survey Report of Xiaojiahegongshe (L-53-8) and Raohe (L-53-9) (in Chinese). Beijing: Geological Publishing House. 12–39

HBGMR (Heilongjiang Bureau of Geology and Mineral Resources). 1987b. 1:200 000 Regional Geological Survey Report of Zhenbaodao (L-53-14) (in Chinese). Beijing: Geological Publishing House. 14–51

Head Iii J W, Wilson L. 2003. Deep submarine pyroclastic eruptions: theory and predicted landforms and deposits. J Volcanol Geotherm Res, 121: 155–193

Helo C, Clague D A, Dingwell D B, Stix J. 2013. High and highly variable cooling rates during pyroclastic eruptions on Axial Seamount, Juan de Fuca Ridge. J Volcanol Geotherm Res, 253: 54–64

Ichiyama Y, Ishiwatari A. 2005. HFSE-rich picritic rocks from the Mino accretionary complex, southwestern Japan. Contrib Mineral Petrol, 149: 373–387

Ichiyama Y, Ishiwatari A, Kimura J I, Senda R, Miyamoto T. 2014. Jurassic plume-origin ophiolites in Japan: Accreted fragments of oceanic plateaus. Contrib Mineral Petrol, 168: 1019

Iezzi G, Caso C, Ventura G, Vallefuoco M, Cavallo A, Behrens H, Mollo S, Paltrinieri D, Signanini P, Vetere F. 2014. First documented deep submarine explosive eruptions at the Marsili Seamount (Tyrrhenian Sea, Italy): A case of historical volcanism in the Mediterranean Sea. Gondwana Res, 25: 764–774

Ikeda M, Tada R. 2014. A 70 million year astronomical time scale for the deep-sea bedded chert sequence (Inuyama, Japan): Implications for Triassic–Jurassic geochronology. Earth Planet Sci Lett, 399: 30–43

Jiang S. 1999. Chemical and Rb-Sr, Sm-Nd isotopic systematics of tourmaline from the Dachang Sn-polymetallic ore deposit, Guangxi Province, P. R. China. Chemgeol, 157: 49–67

Jiang S Y, Palmer M R, Slack J F, Shaw D R. 1999. Boron isotope systematics of tourmaline formation in the Sullivan Pb-Zn-Ag deposit, British Columbia, Canada. Chemgeol, 158: 131–144

Jones C E, Jenkyns H C. 2001. Seawater strontium isotopes, oceanic anoxic events, and seafloor hydrothermal activity in the Jurassic and Cretaceous. Am J Sci, 301: 112–149

Kamata Y, Maezawa A, Hara H, Ueno K, Hisada K, Sardsud A, Charoentitirat T, Charusiri P. 2012. Basaltic activity preserved in an Upper Permian radiolarian chert from the Paleo-Tethys in the Inthanon Zone, northern Thailand. J Asian Earth Sci, 61: 51–61

Kano K, Yamamoto T, Ono K. 1996. Subaqueous eruption and emplacement of the Shinjima Pumice, Shinjima (Moeshima) Island, Kagoshima Bay, SW Japan. J Volcanol Geotherm Res, 71: 187–206

Kimura G, Sakakibara M, Okamura M. 1994. Plumes in central Panthalassa? Deductions from accreted oceanic fragments in Japan. Tectonics, 13: 905–916

Kokelaar P, Busby C. 1992. Subaqueous explosive eruption and welding of pyroclastic deposits. Science, 257: 196–201

Korte C, Kozur H W, Bruckschen P, Veizer J. 2003. Strontium isotope evolution of Late Permian and Triassic seawater. Geochim Cosmochim Acta, 67: 47–62

Kushiro I. 1960. Si-Al relation in clinopyroxenes from igneous rocks. Am J Sci, 258: 548–554

Kutterolf S, Schindlbeck J C, Scudder R P, Murray R W, Pickering K T, Freundt A, Labanieh S, Heydolph K, Saito S, Naruse H, Underwood M B, Wu H. 2014. Large volume submarine ignimbrites in the Shikoku Basin: An example for explosive volcanism in the Western Pacific during the Late Miocene. Geochem Geophys Geosyst, 15: 1837–1851

Le Bas M J. 1962. The role of aluminum in igneous clinopyroxenes with relation to their parentage. Am J Sci, 260: 267–288

Ludwig K R. 2001. Squid 1.03 A User's Manual. Berkeley Geochronol Cent Spec Publ, doi: http://www.bgc.org/isoplot_etc/squid.html

Ludwig K R. 2003. User's Manual for Isoplot 3.0: A geochronological toolkit for Microsoft Excel. Berkeley Geochronol Center Spec Publ, doi: http://www.bgc.org/isoplot_etc/isoplot.html

Ma J L, Wei G J, Xu Y G, Long W G, Sun W D. 2007. Mobilization and redistribution of major and trace elements during extreme weathering of basalt in Hainan Island, South China. Geochim Cosmochim Acta, 71: 3223–3237

McBirney A R. 1963. Factors governing the nature of submarine volcanism. Bull Volcanol, 26: 455–469

Mielke P, Nehler M, Bignall G, Sass I. 2015. Thermo-physical rock properties and the impact of advancing hydrothermal alteration — A case study from the Tauhara geothermal field, New Zealand. J Volcanol Geotherm Res, 301: 14–28

Mizutani S, Kojima S. 1992. Mesozoic radiolarian biostratigraphy of Japan and collage tectonics along the eastern continental margin of Asia. Palaeogeogr Palaeoclimatol Palaeoecol, 96: 3–22

Muller R D, Dutkiewicz A, Seton M, Gaina C. 2013. Seawater chemistry driven by supercontinent assembly, breakup, and dispersal. Geology, 41: 907–910

Nelson D R, Myers J S, Nutman A P. 1995. Chronology and evolution of the Middle Proterozoic Albany-Fraser Orogen, Western Australia. Australian J Earth Sci, 42: 481–495

Pallister J S, Budahn J R, Murchey B L. 1989. Pillow basalts of the Angayucham terrane: Oceanic plateau and island crust accreted to the Brooks Range. J Geophys Res, 94: 15901–15923

Porreca M, Cifelli F, Soriano C, Giordano G, Romano C, Conticelli S, Mattei M. 2014. Hyaloclastite fragmentation below the glass transition: An example from El Barronal submarine volcanic complex (Spain). Geology, 42: 87–90

Resing J A, Rubin K H, Embley R W, Lupton J E, Baker E T, Dziak R P, Baumberger T, Lilley M D, Huber J A, Shank T M, Butterfield D A, Clague D A, Keller N S, Merle S G, Buck N J, Michael P J, Soule A, Caress D W, Walker S L, Davis R, Cowen J P, Reysenbach A L, Thomas H. 2011. Active submarine eruption of boninite in the northeastern Lau Basin. Nat Geosci, 4: 799–806

Richter F M, Rowley D B, Depaolo D J. 1992. Sr isotope evolution of seawater: The role of tectonics. Earth Planet Sci Lett, 109: 11–23

Safonova I Y, Santosh M. 2014. Accretionary complexes in the Asia-Pacific region: Tracing archives of ocean plate stratigraphy and tracking mantle plumes. Gondwana Res, 25: 126–158

Safonova I Y, Utsunomiya A, Kojima S, Nakae S, Tomurtogoo O, Filippov A N, Koizumi K. 2009. Pacific superplume-related oceanic basalts hosted by accretionary complexes of Central Asia, Russian Far East and Japan. Gondwana Res, 16: 587–608

Schneider J L. 2000. Volcaniclastic sedimentation in submarine settings: products and processes. In: Leyrit H, Montenat C, eds. Volcaniclastic Rocks From Magmas to Sediments. Amsterdam: Gordon and Breach Science Publishers. 175–192

Sheridan M F, Wohletz K H. 1981. Hydrovolcanic Explosions: The Systematics of Water-Pyroclast Equilibration. Science, 212: 1387–1389

Shervais J W. 1982. Ti-V plots and the petrogenesis of modern and ophiolitic lavas. Earth Planet Sci Lett, 59: 101–118

Sohn R A, Willis C, Humphris S, Shank T M, Singh H, Edmonds H N, Kunz C, Hedman U, Helmke E, Jakuba M, Liljebladh B, Linder J, Murphy C, Nakamura K I, Sato T, Schlindwein V, Stranne C, Tausenfreund M, Upchurch L, Winsor P, Jakobsson M, Soule A. 2008. Explosive volcanism on the ultraslow-spreading Gakkel ridge, Arctic Ocean. Nature, 453: 1236–1238

Stanton R J, Alderson J M. 2013. Limestone interbedded with submarine volcanics: the Early–Middle Miocene Conejo Volcanics, California. Facies, 59: 467–480

Stern R A. 2001. A new isotopic and trace-element standard for the ion microprobe: preliminary thermal ionization mass spectrometry (TIMS) U-Pb and electron-microprobe data. Rediogenic Age and Isotopic Studies: Report 14. Geol Surv Canada Curr Res, 2001-F1: 1–11

Sun M D, Xu Y G, Wilde S A, Chen H L. 2015. Provenance of Cretaceous trench slope sediments from the Mesozoic Wandashan Orogen, NE China: Implications for determining ancient drainage systems and tectonics of the Paleo-Pacific. Tectonics, 34: 1269–1289

Sun S S, McDonough W F. 1989. Chemical and isotopic systematics of oceanic basalts: Implications for mantle composition and processes. In: Saunders A D, Norry M J, eds. Magmatism in the Ocean Basins. Geol Soc Spec Publ London. 313–345

Timm C, Hoernle K, Werner R, Hauff F, van den Bogaard P, Michael P, Coffin M F, Koppers A. 2011. Age and geochemistry of the oceanic Manihiki Plateau, SW Pacific: New evidence for a plume origin. Earth Planet Sci Lett, 304: 135–146

Utsunomiya A, Suzuki N, Ota T. 2008. Preserved paleo-oceanic plateaus in accretionary complexes: Implications for the contributions of the Pacific superplume to global environmental change. Gondwana Res, 14: 115–125

Wakita K. 2012. Mappable features of mélanges derived from Ocean Plate Stratigraphy in the Jurassic accretionary complexes of Mino and Chichibu terranes in Southwest Japan. Tectonophysics, 568-569: 74–85

Wang Z H, Ge W C, Yang H, Zhang Y L, Bi J H, Tian D X, Xu W L. 2015. Middle Jurassic oceanic island igneous rocks of the Raohe accretionary complex, northeastern China: Petrogenesis and tectonic implications. J Asian Earth Sci, 111: 120–137

White J D L, Smellie J L, Clague D A. 2003. Explosive Subaqueous Volcanism. American Geophysical Union. 1–20

Wierzbowski H, Anczkiewicz R, Bazarnik J, Pawlak J. 2012. Strontium isotope variations in Middle Jurassic (Late Bajocian–Callovian) seawater: Implications for Earth's tectonic activity and marine environments. Chem Geol, 334: 171–181

Wohletz K H, Sheridan M F. 1983. Hydrovolcanic explosions. 2. Evolution of basaltic tuff rings and tuff cones. Am J Sci, 283: 385–413

Wright I C. 2001. In situ modification of modern submarine hyaloclastic/ pyroclastic deposits by oceanic currents: An example from the Southern Kermadec arc (SW Pacific). Mar Geol, 172: 287–307

Xenophontos C, Osozawa S. 2004. Travel time of accreted igneous assemblages in western Pacific orogenic belts and their associated sedimentary rocks. Tectonophysics, 393: 241–261

Xu Y G, Ma J L, Frey F A, Feigenson M D, Liu J F. 2005. Role of lithosphere—Asthenosphere interaction in the genesis of Quaternary alkali and tholeiitic basalts from Datong, western North China Craton. Chem Geol, 224: 247–271

Zhou J B, Cao J L, Wilde S A, Zhao G C, Zhang J J, Wang B. 2014. Paleo-Pacific subduction-accretion: Evidence from Geochemical and U-Pb zircon dating of the Nadanhada accretionary complex, NE China. Tectonics, 33: 2444–2466

(Responsibility editor: Guochun ZHAO)